Supporting Information

Xinyao Zhang[a], Zhen Sun[a*], Ruiying Lu[a], Jiarui Xu[a], Hongyu Xu[a], Wei Xu[b]

[a] *Key Laboratory for Microstructural Material Physics of Hebei Province, School of Science, Yanshan University, Qinhuangdao 066004, P.R. China.*

[b] *School of Electrical Engineering, Yanshan University, Qinhuangdao, 066004, China.*

**zsun@ysu.edu.cn*

Table S1 Refine data and lattice parameters

Formula	CLSO:0.02Dy^{3+}	CLSO:0.02Dy^{3+},0.03Eu^{3+}	CLSO:0.02Dy^{3+},0.03Tb^{3+}
Space group	*P*63/*m*	*P*63/*m*	*P*63/*m*
Volume（$Å^3$）	576.862	575.715	574.959
Crystal system	hexagonal	hexagonal	hexagonal
Lattice parameters（Å）	a= 9.65564 b=9.65564 c=7.14463	a= 9.65045 b=9.65045 c=7.13809	a=9.64679 b=9.64679 c=7.13413
R_{wp} (%)	8.65	7.92	8.52
R_p (%)	6.01	5.37	6.03
χ^2 (%)	5.76	5.79	6.21

Table S2 Lattice parameters of CLSO:Dy^{3+}, Dy^{3+}/Eu^{3+}, Dy^{3+}/Tb^{3+} from room temperature to 523 K.

Temperature, K	a=b, Å	c, Å	V, $Å^3$
CLSO:0.02Dy^{3+}			
303	9.65509	7.14464	576.729
363	9.65831	7.14714	577.385
423	9.66679	7.15251	578.834
473	9.67139	7.15524	579.606
523	9.67942	7.16007	580.961
CLSO:0.02Dy^{3+}, 0.03Eu^{3+}			
303	9.65335	7.14022	576.233
363	9.65675	7.14189	576.694
423	9.66182	7.14568	577.686
473	9.66850	7.14889	578.678
523	9.67328	7.15155	579.533
CLSO:0.02Dy^{3+}, 0.03Tb^{3+}			
303	9.64790	7.13150	574.880
363	9.65318	7.13435	575.738
423	9.65751	7.13638	576.421
473	9.66141	7.13913	577.106
523	9.66803	7.14291	578.163

Table S3 Unit-cell parameters determined using Rietveld refinement.

Compounds	x (Å)	y (Å)	z (Å)	Wyckoff position	U_{iso}
$CaLa_4Si_3O_{13}$:0.02Dy^{3+}					
Ca1/La1/Dy1	0.3333	0.6667	0.0037	4f	0.0121
Ca2/La2/Dy2	0.2451	0.0137	0.2500	6h	0.0095
Si	0.3760	0.4053	0.2500	6h	0.0175
O(1)	0.4663	0.5855	0.2500	6h	0.0228
O(2)	0.4810	0.3367	0.2500	6h	0.0048
O(3)	0.2625	0.3455	0.0750	12i	0.0177
O(4)	0.0000	0.0000	0.2500	2a	0.0131
$CaLa_4Si_3O_{13}$:0.02Dy^{3+}, 0.03Eu^{3+}					
Ca1/La1/Dy1/Eu1	0.3333	0.6667	0.0037	4f	0.0101
Ca2/La2/Dy2/Eu2	0.2450	0.0133	0.2500	6h	0.0006
Si	0.3729	0.4031	0.2500	6h	0.0129
O(1)	0.4665	0.5930	0.2500	6h	0.0221
O(2)	0.4845	0.3310	0.2500	6h	0.0038
O(3)	0.2563	0.3423	0.0748	12i	0.0161
O(4)	0.0000	0.0000	0.2500	2a	0.0125
$CaLa_4Si_3O_{13}$:0.02Dy^{3+}, 0.03Tb^{3+}					
Ca1/La1/Dy1/Tb1	0.3333	0.6667	0.0033	4f	0.0120
Ca2/La2/Dy2/Tb2	0.2453	0.0135	0.2500	6h	0.0077
Si	0.3743	0.4046	0.2500	6h	0.0154
O(1)	0.4677	0.5948	0.2500	6h	0.0224
O(2)	0.4796	0.3408	0.2500	6h	0.0070
O(3)	0.2607	0.3433	0.0737	12i	0.0210
O(4)	0.0000	0.0000	0.2500	2a	0.0100

Table S4 Details of the LIRs fit parameters in CLSO:Dy^{3+}, Dy^{3+}/Eu^{3+}, Dy^{3+}/Tb^{3+}

LIR	fitted equation	R^2
$CaLa_4Si_3O_{13}$:0.02Dy^{3+}		
$B1/B2_{(1)}$	LIR = 2.12 × exp(-1216.11/T)	99.6%
$B1/B2_{(2)}$	LIR = 2.83 × exp(-1216.71/T)	99.6%
B1/Y2	LIR = 1.19 × exp(-961.57/T)	99.7%
LIR*	LIR = 10.58 × exp(-3628.23/T)	99.9%
$CaLa_4Si_3O_{13}$:0.02Dy^{3+}, 0.03Eu^{3+}		
$B1/B2_{(1)}$	LIR = 2.07 × exp(-1052.64/T)	98.9%
$B1/B2_{(2)}$	LIR = 2.74 × exp(-1057.89/T)	99.2%
B1/Y2	LIR = 1.80 × exp(-955.69/T)	98.4%
B1/Eu1	LIR = 1.73 × exp(-1102.10/T)	97.0%
LIR*	LIR = 137.96 × exp(-5248.13/T)	99.9%
$CaLa_4Si_3O_{13}$:0.02Dy^{3+}, 0.03Tb^{3+}		
$B1/B2_{(1)}$	LIR = 0.82 × exp(-697.33/T)	99.3%
$B1/B2_{(2)}$	LIR = 0.78 × exp(-789.60/T)	99.6%
B1/Tb1	LIR = 0.67 × exp(-784.28/T)	99.7%
B1/Y2	LIR = 0.34 × exp(-606.21/T)	99.6%
B1/Tb2	LIR = 2.46 × exp(-645.89/T)	99.4%
LIR*	LIR = 0.48 × exp(-3657.80/T)	99.9%

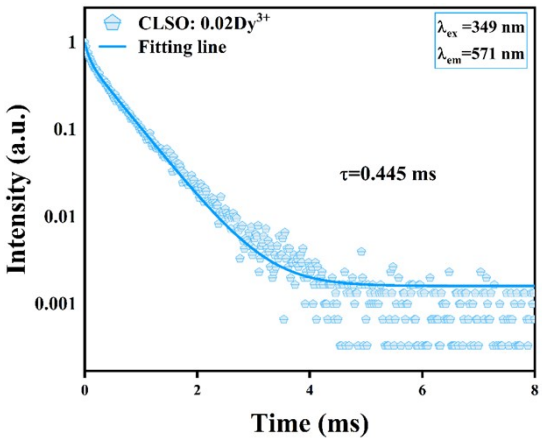

Fig. S1 Luminescence lifetime curve of $^4F_{9/2}\rightarrow{}^6H_{13/2}$ transition of $0.02Dy^{3+}$ doped CLSO phosphor, recorded following excitation at 349 nm.

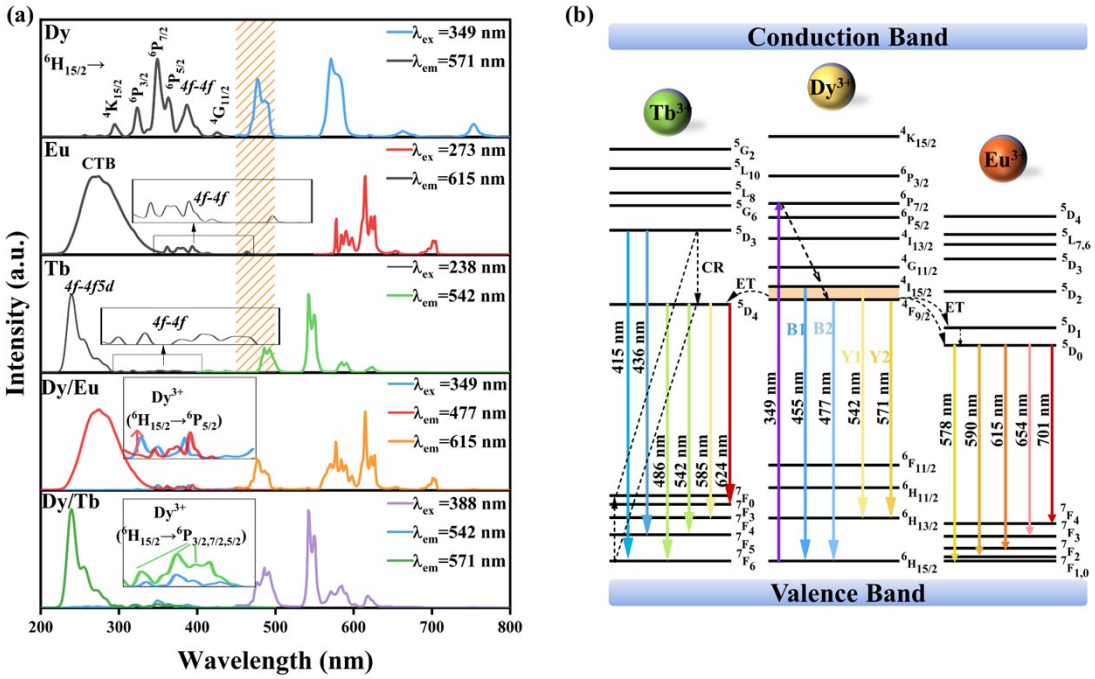

Fig. S2 (a) The PLE and PL spectra of Dy^{3+}, Eu^{3+}, Tb^{3+} ions singly doped and Dy^{3+}/Eu^{3+}, Dy^{3+}/Tb^{3+}co-doped CLSO phosphors. (b) Energy level diagram and energy transfer model of Dy^{3+}, Tb^{3+} and Eu^{3+}.

After the electrons in $^6H_{15/2}$ level of the Dy^{3+} are pumped to the $^6P_{7/2}$ excited state, part of the electrons is non-radiatively relaxed to the $^4F_{9/2}$ excited state and the characteristic emission of Dy is produced. Meanwhile, some of the electrons on the excited $^4F_{9/2}$ energy level of Dy^{3+} transfer to the neighboring Eu^{3+} ($^5D_0$) state and Tb^{3+} ($^5D_4$) level. The excited $^5D_0$ electrons then relax to the $^7F_0$, $^7F_1$, $^7F_2$, $^7F_3$, and $^7F_4$ levels, producing emissions of 578 nm, 590 nm, 615 nm, 654 nm, and 701 nm, respectively. Similarly, electron transitions from Tb^{3+} $^5D_4$ levels to ^7F_J (J=6,5,4,3) produce emissions of 486 nm, 542 nm, 585 nm, and 624 nm, respectively.

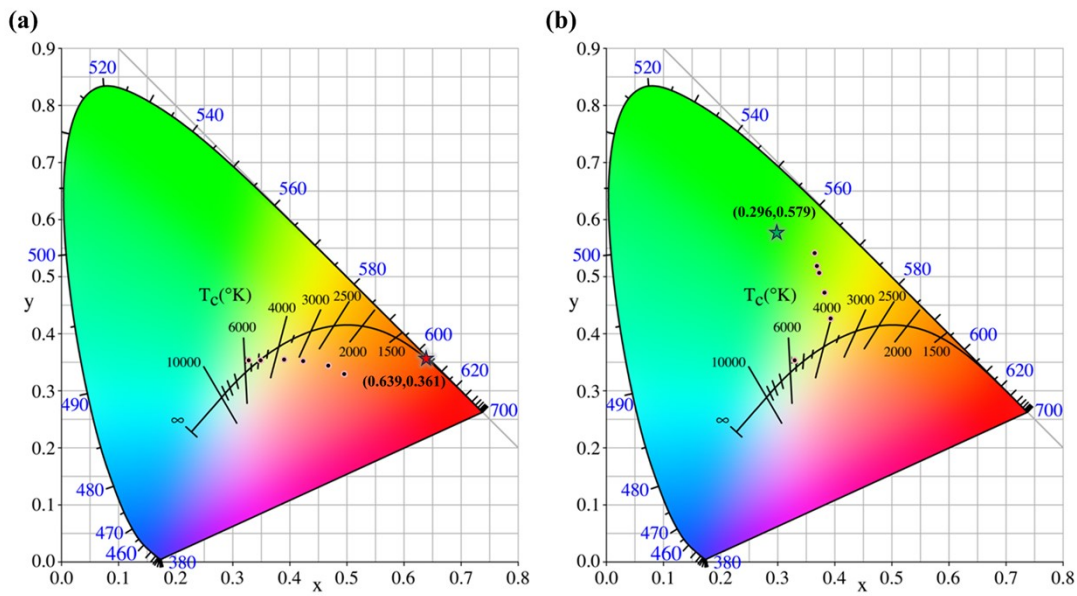

Fig. S3 CIE chromaticity coordinates for (a) CLSO:0.09Eu^{3+} and CLSO:0.02Dy^{3+},xEu^{3+} ($0 \leq x \leq 0.09$) samples. (b) CIE chromaticity coordinates for CLSO:0.11Tb^{3+} and CLSO:0.02Dy^{3+},xTb^{3+} ($0 \leq x \leq 0.09$) samples.

The color purity (C.P.) of the samples is calculated as follows: $C.P. = \frac{\sqrt{(x_s - x_i)^2 + (y_s - y_i)^2}}{\sqrt{(x_d - x_i)^2 + (y_d - y_i)^2}} \times 100\%$ where (x_d, y_d) are the coordinates of the dominant wavelength, (x_s, y_s) are the coordinates of the sample point, and (x_i, y_i) are the coordinates of the white light. In this study, (x_d, y_d)= (0.444, 0.554), (0.670, 0.330) or (0.244, 0.743) for a dominant wavelength of 571 nm, 615 nm and 542 nm, and (x_i, y_i)=(0.3101, 0.3162).[1-3] The C.P. of optimal single doped samples with Dy^{3+}, Eu^{3+} and Tb^{3+} are 21.1%, 92.2% and 60.9%, respectively. Based on the CIE results, an increase of Eu^{3+} and Tb^{3+} concentrations could result in the color coordinates of CLSO:Dy^{3+}/Eu^{3+} and CLSO:Dy^{3+}/Tb^{3+} shifting to the ideal red and green chromaticity. When the concentration of co-doped Eu^{3+} and Tb^{3+} reaches 0.09, the C.P. values of the samples increase to 51.9% and 53.6%, respectively.

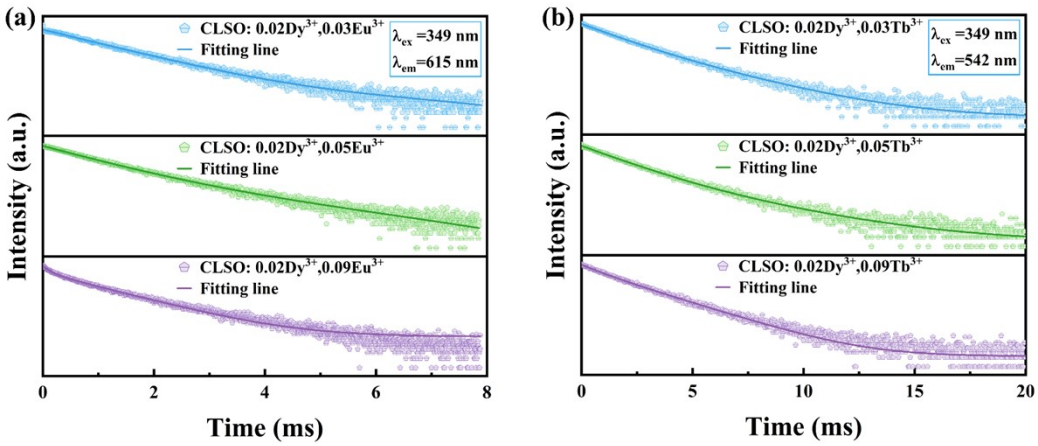

Fig. S4 The decay curves of (a) Eu^{3+} in the CLSO:0.02Dy^{3+},xEu^{3+} (x=0.03,0.05,0.09) and (b) Tb^{3+} in the CLSO:0.02Dy^{3+},xTb^{3+} (x=0.03,0.05,0.09) phosphors.

Because of the ET process, the lifetime of Eu^{3+} increases from 0.98 ms to 1.16 ms, while decreasing to 0.87 ms when the Eu^{3+} concentration is increased to 0.09.[4] The lifetime of Tb^{3+} also exhibits a similar pattern, increasing from 1.95 ms to 2.01 ms and subsequently decreasing to 1.82 ms due to concentration quenching.[5]

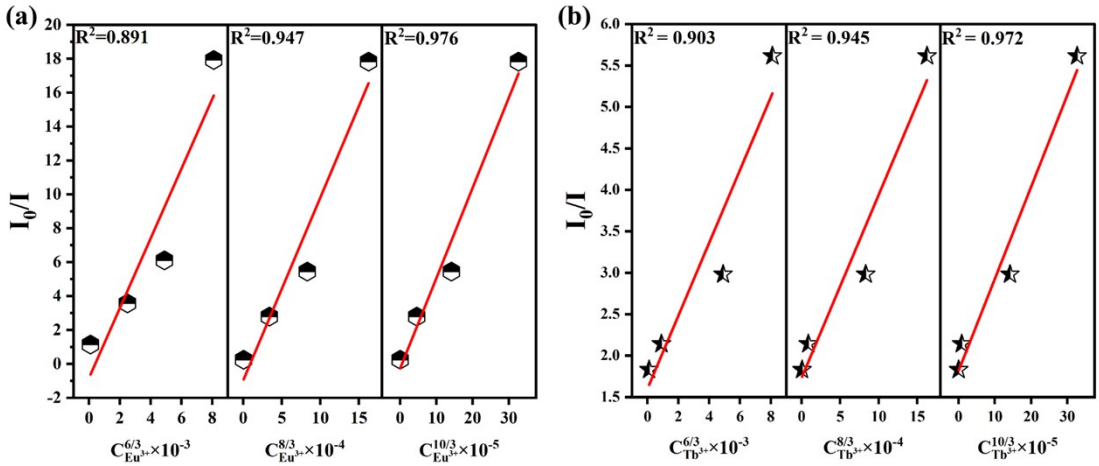

Fig. S5 Dependence of (I_0/I) of Dy^{3+} on $C^{\alpha/3}$ (α=6, 8, 10) in (a) CLSO:0.02Dy^{3+}, 0.03Eu^{3+} and (b) CLSO:0.02Dy^{3+},0.03Tb^{3+}.

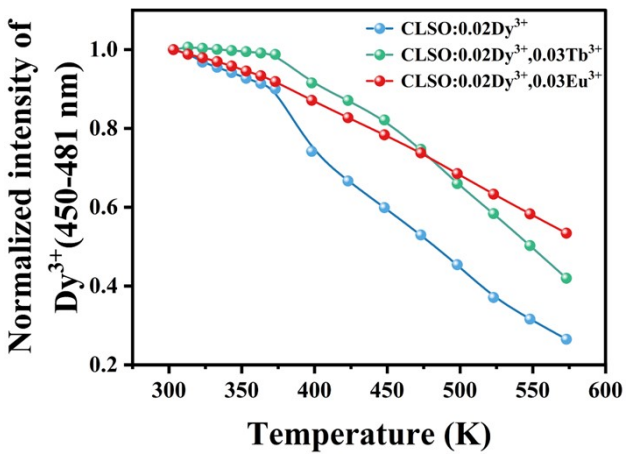

Fig. S6 Normalized integral luminescence intensity of Dy^{3+} 450-481nm in three samples as a function of temperature.

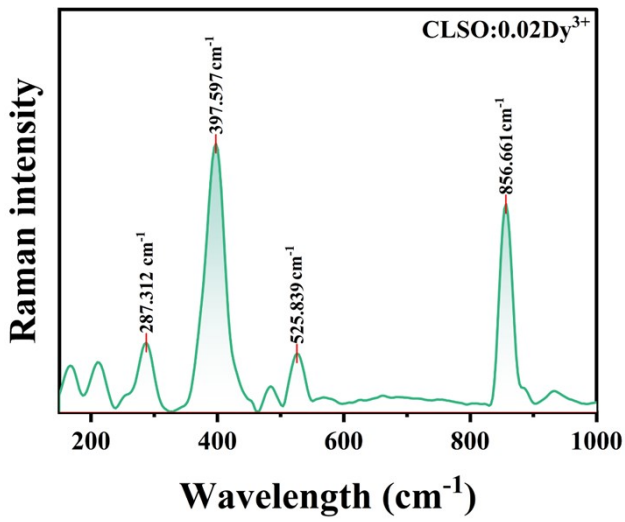

Fig. S7 Raman spectrum for CLSO:0.02Dy^{3+}.

The peaks above 350 cm^{-1} are assigned to internal modes of SiO_4 tetrahedral units. The symmetric stretching mode υ1 of SiO_4 tetrahedral is assigned to the strong peak at about 856 cm^{-1}, while the asymmetric mode υ3 is responsible for the weak band at about 930cm1.The peak at about 526 cm^{-1} is attributed to the asymmetric bending υ4 mode and the strongest peak at about 398 cm^{-1} belongs to the symmetric bending υ2 mode. The external modes involving translations and rotational oscillations of the SiO_4, LaO_7 and LaO_9 units are expected to contribute to the Raman peaks at below 350 cm^{-1}.[6]

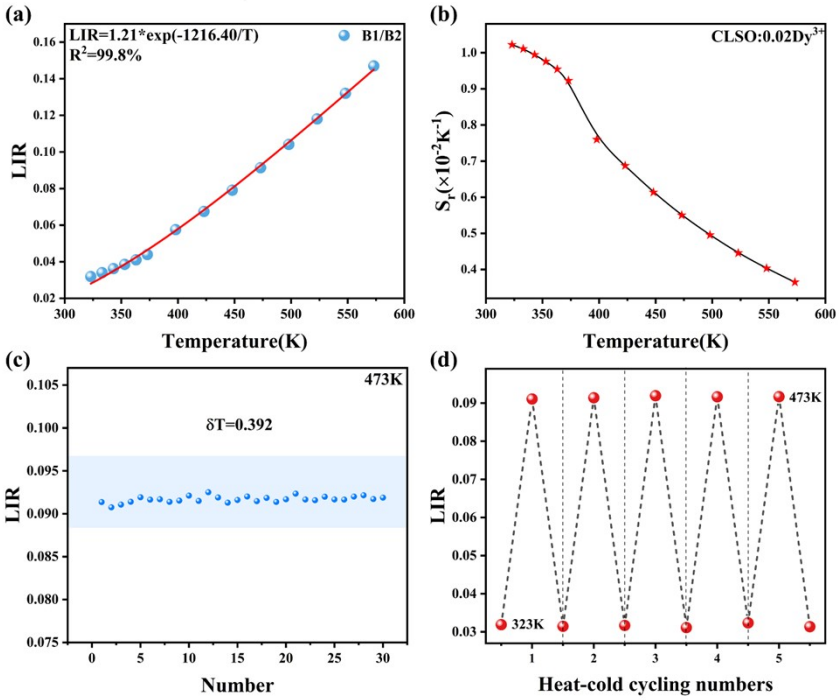

Fig. S8 (a) Evolution of LIR(B1/B2) under various temperatures for CLSO:0.02Dy^{3+}. (b) and (c) The S_r and δT values of CLSO:0.02Dy^{3+} phosphor. (d) LIR values of the temperature-cycle measurements.

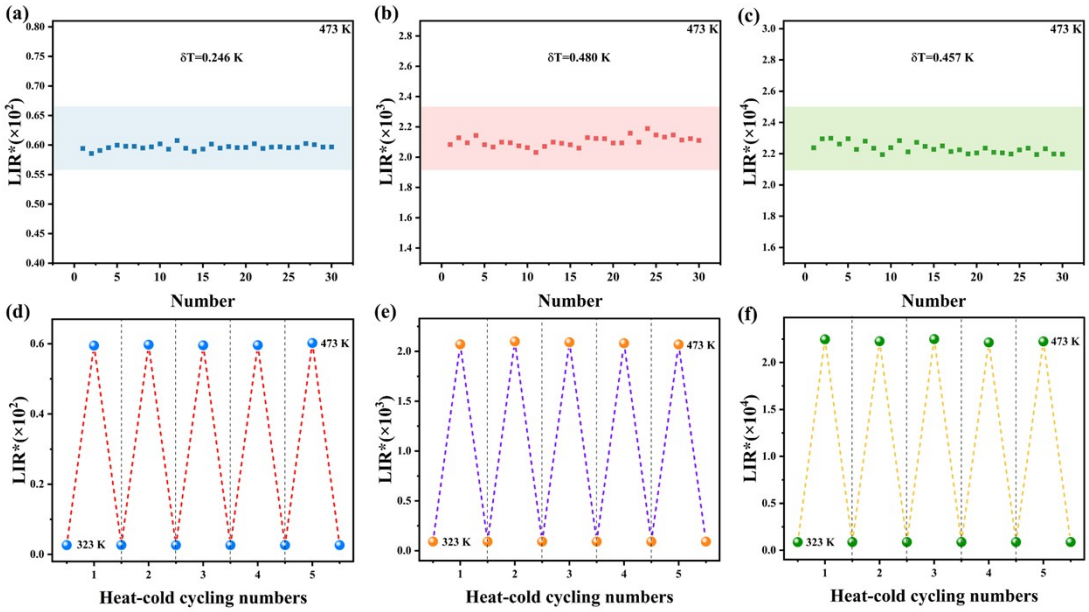

Fig. S9 Fluctuation of LIR* and the calculated temperature resolution δT at 473 K of (a) CLSO:0.02Dy^{3+}, (b) 0.02Dy^{3+},0.03Eu^{3+}, (c) 0.02Dy^{3+},0.03Tb^{3+} phosphors. (d-f) LIR* values of the temperature-cycle measurements.

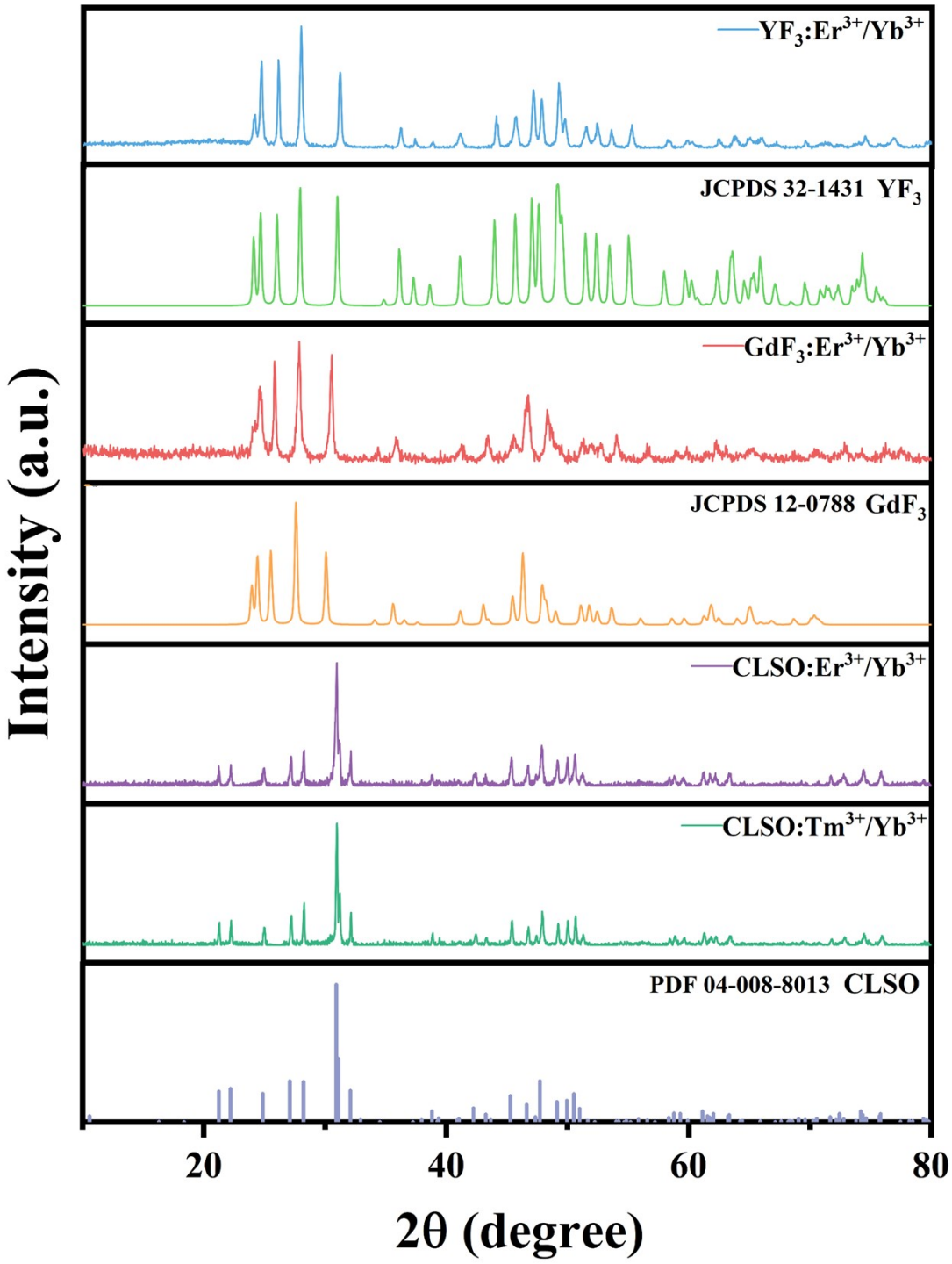

Fig. S10 XRD patterns of GdF_3:0.01Er^{3+},0.05Yb^{3+}, YF_3:0.01Er^{3+},0.05Yb^{3+}, CLSO:0.01Er^{3+},0.05Yb^{3+} and CLSO:0.003Tm^{3+},0.05Yb^{3+} samples.

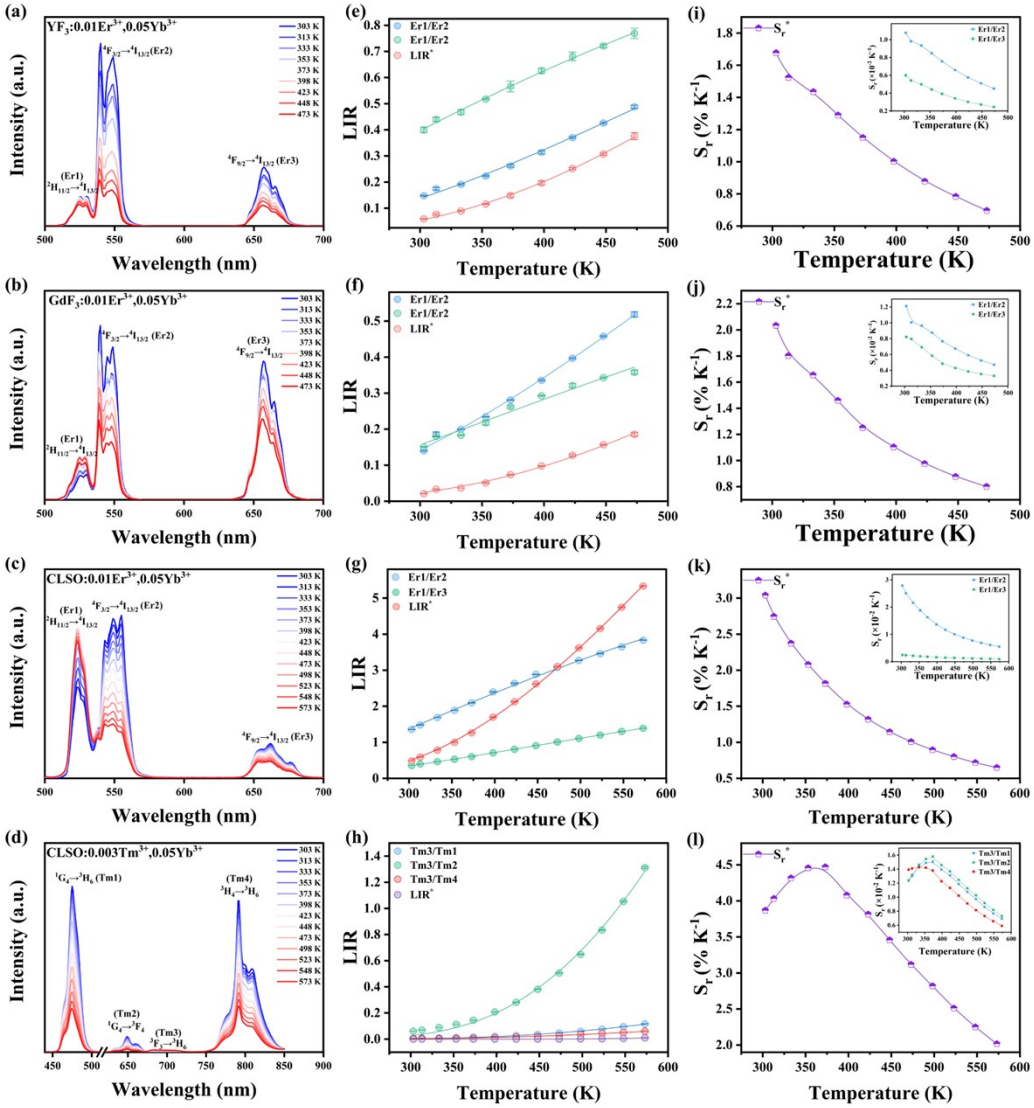

Fig. S11 (a-d) Thermal evolution spectra of $0.01Er^{3+}$ and $0.05Yb^{3+}$ co-doped GdF_3/YF_3/CLSO and CLSO:$0.003Tm^{3+}$, $0.05Yb^{3+}$ phosphors. (e-h) Evolution of LIRs and (i-l) the relative sensitivities under various temperatures.

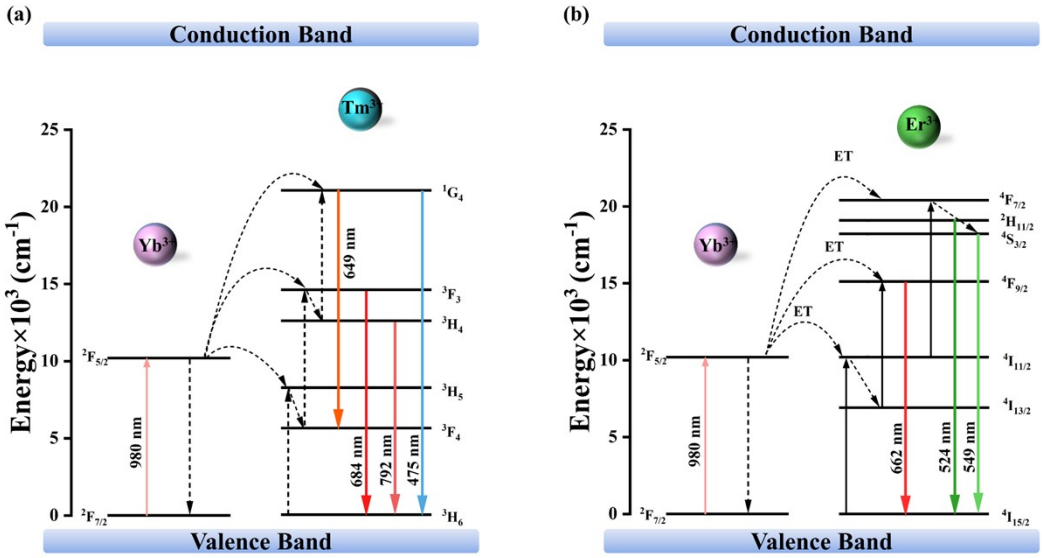

Fig. S12 Energy level diagrams of Er^{3+}, $Tm^{3+}$and possible up-conversion mechanism.[7]

References

1 K. A. Denault, J. Brgoch, M. W. Gaultois, A. Mikhailovsky, R. Petry, H. Winkler, S. P. DenBaars, and R. Seshadri, Microwave-assisted synthesis of GdOF:Eu^{3+}/Tb^{3+} ultrafine phosphor powders suitable for advanced forensic and security ink applications, *J. Colloid Interface Sci.*, 2023, **641**, 1014–1032.

2 H. Tang, X. Zhang, L. Cheng, X. Mi and Q. Liu, Thermally stable and highly efficient red-emitting Eu^{3+}-doped $Cs_3GdGe_3O_9$ phosphors for WLEDs: non-concentration quenching and negative thermal expansion, *Light-Sci. Appl.*, 2021, **10**, 29.

3 T. Otsuka, R. Oka, and T. Hayakawa, Eu^{3+} Site Distribution and Local Distortion of Photoluminescent Ca_3WO_6:(Eu^{3+},K^+) Double Perovskites as High-Color-Purity Red Phosphors, *Adv. Sci.*, 2023, **10**, 2302559.

4 Y. Liu, J. Wang, X. Liu, H. Zhang and H. Liu, Energy transfer and luminescence properties of $BaSr_2Gd_{1-x}M_x(PO_4)_3$ (M= Dy, Tm, Eu) phosphors for warm white UV LEDs, *Opt. Mater.*, 2019, **95**, 109194.

5 Y. Zhang, L. Mei, S. M. Aksenov, H. Liu, D. Zhang and Z. Huang, New apatite-type phosphor $Ca_9La(PO_4)_5(SiO_4)F_2$:Tb^{3+},Dy^{3+} with improved color rendering index, *J. Am. Ceram. Soc.*, 2020, **103**, 2602-2609.

6 J. Song, K. Song, J. Wei, H. Lin, J. Xu, J. Wu and W. Su, Microstructure characteristics and microwave dielectric properties of calcium apatite ceramics as microwave substrates, *J. Alloy. Compd.*, 2018, **731**, 264-270.

7 K. Zhu, H. Xu, Z. Wang and Z. Fu, Lanthanide-doped lead-free double perovskite La_2MgTiO_6 as ultra-bright multicolour LEDs and novel self-calibrating partition optical thermometer, *Inorg. Chem. Front.*, 2023, **10**, 3383-3395.